One-dimensional particle simulation of the filamentation instability: Electrostatic field driven by the magnetic pressure gradient force

M. E. Dieckmann,[1] I. Kourakis,[1] M. Borghesi,[1] and G. Rowlands[2]
[1]*Centre for Plasma Physics, Queen's University Belfast, Belfast BT7 1NN, United Kingdom*
[2]*Department of Physics, Warwick University, Coventry CV4 7AL, United Kingdom*

(Received 23 April 2009; accepted 9 June 2009; published online 7 July 2009)

Two counterpropagating cool and equally dense electron beams are modeled with particle-in-cell simulations. The electron beam filamentation instability is examined in one spatial dimension, which is an approximation for a quasiplanar filament boundary. It is confirmed that the force on the electrons imposed by the electrostatic field, which develops during the nonlinear stage of the instability, oscillates around a mean value that equals the magnetic pressure gradient force. The forces acting on the electrons due to the electrostatic and the magnetic field have a similar strength. The electrostatic field reduces the confining force close to the stable equilibrium of each filament and increases it farther away, limiting the peak density. The confining time-averaged total potential permits an overlap of current filaments with an opposite flow direction. © *2009 American Institute of Physics*. [DOI: 10.1063/1.3160629]

The electron beam filamentation instability (FI) generates magnetic fields in energetic astrophysical[1–5] and solar flare plasmas[6] and in laser plasma interactions[7,8] if the beam speeds $|\mathbf{v}_b|$ are comparable to c and if the densities of the counterstreaming beams are similar.[9] It has been investigated with one-dimensional (1D) particle-in-cell (PIC) and Vlasov simulations[10,11] and with two-dimensional (2D) PIC simulations.[12,13] The counterstreaming electron beam instability has also been examined with a three-dimensional PIC simulation.[14] Mobile ions and a guiding magnetic field have been taken into account[10,13,15] and statistical properties of the FI have been obtained.[16–18]

The FI triggers the growth of waves with the wave vectors $\mathbf{k} \perp \mathbf{v}_b$ over a wide band of $k=|\mathbf{k}|$, where the wave numbers k are of the order of the inverse electron skin depth. The electrons are deflected by the magnetic field perturbation, and electrons moving in opposite directions separate in space. The net current of these flow channels amplifies the initial perturbation and, thus, the tendency to form current channels. The magnetic field amplitude grows exponentially and it saturates by the magnetic trapping of electrons.[11] The FI can also couple nonlinearly to electrostatic waves.[10,13,18] It has been suggested[15,18] that it is the magnetic pressure gradient that gives rise to the electrostatic field that grows when the FI saturates, but it has not yet been demonstrated quantitatively. This is the purpose of this paper.

We consider here the FI driven by equally dense and warm electron beams, which have a Maxwellian velocity distribution in their rest frame. This case is important because the growth rate of the FI is highest relative to the competing mixed mode and two-stream instabilities for symmetric beams.[9] We study the FI with a PIC simulation code[19] that is based on the electromagnetic and relativistic virtual particle-mesh method.[20]

The FI is modeled in a simulation reference frame, in which both beams move into opposite directions at the speed modulus $v_b=0.3c$. We isolate the FI by selecting a 1D simulation box that is oriented orthogonally to the beam velocity vector $\mathbf{v}_b$ and we resolve all velocity components. This is an approximation for a quasiplanar boundary between filaments with an oppositely directed electron flow. They occur in warm plasmas if the confining magnetic field cannot overcome the thermal pressure and they are characterized by planar magnetic fields.[15,17,21] The periodic boundary conditions of the short simulation box result in the development of only one pair of filaments. The restriction to one dimension inhibits the merging of the filaments[12] and we can analyze the relation between the electric and magnetic fields of the quasistationary filaments.

Beam 1 has the mean speed $\boldsymbol{v}_{b1}=v_b\boldsymbol{z}$ and beam 2 has $\boldsymbol{v}_{b2}=-v_b\boldsymbol{z}$. Both beams are spatially uniform and have a Maxwellian velocity distribution in their respective rest frame with a thermal speed $v_{\rm th}=(k_bT/m_e)^{0.5}$ of $v_b/v_{\rm th}=18$. An immobile positive charge background corresponding to infinitely heavy ions cancels the electron charge and the current contributions of both beams cancel to zero in the selected reference frame. We can thus set initially $\mathbf{E}=0$ and $\mathbf{B}=0$. The 1D simulation box with its periodic boundary conditions is aligned with the $\boldsymbol{x}$-direction. We thus denote positions by the scalar x. The plasma frequency of each beam with the number density n_e is $\omega_p=(e^2n_e/m_e\epsilon_0)^{0.5}$. The total plasma frequency $\Omega_p=\sqrt{2}\omega_p$. The electric and magnetic fields are normalized to $\boldsymbol{E}_N=e\boldsymbol{E}/cm_e\Omega_p$ and $\boldsymbol{B}_N=e\boldsymbol{B}/m_e\Omega_p$ and the current to $\boldsymbol{J}_N=\boldsymbol{J}/2n_eec$. The physical position and time are normalized as $x_N=x/\lambda_s$ with the electron skin depth $\lambda_s=c/\Omega_p$ and $t_N=t\Omega_p$. We drop the index N and $x,t,\boldsymbol{E},\boldsymbol{B},\boldsymbol{J}$ are specified in normalized units.

The box length $L=0.89$ is resolved by $N_g=500$ grid cells with the length Δ_x. The simulation time $t_S=125$. The phase space distributions $f_1(x,\boldsymbol{p})$ of beam 1 and $f_2(x,\boldsymbol{p})$ of beam 2 are each sampled by $N_p=6.05\times10^7$ computational particles (CPs). The total phase space density is defined as $f(x,\boldsymbol{p})=f_1(x,\boldsymbol{p})+f_2(x,\boldsymbol{p})$.

The electrons and their microcurrents are redistributed

 © 2009 American Institute of Physics

Downloaded 23 Aug 2011 to 143.117.13.152. Redistribution subject to AIP license or copyright; see http://pop.aip.org/about/rights_and_permissions

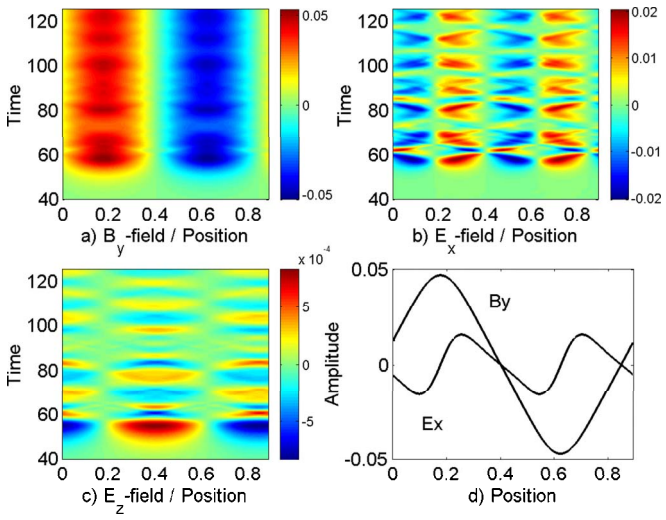

FIG. 1. (Color online) (a)–(c) show B_y, E_x, and E_z. All fields are stationary in space and B_y is quasistationary also in time for $t>56$. E_x oscillates in space twice as fast as B_y and both are spatially correlated for $55<t<125$. The phase of E_z is shifted by 90° relative to that of B_y and it is damped. The B_y, E_x fields at $t=56$ are compared in (d).

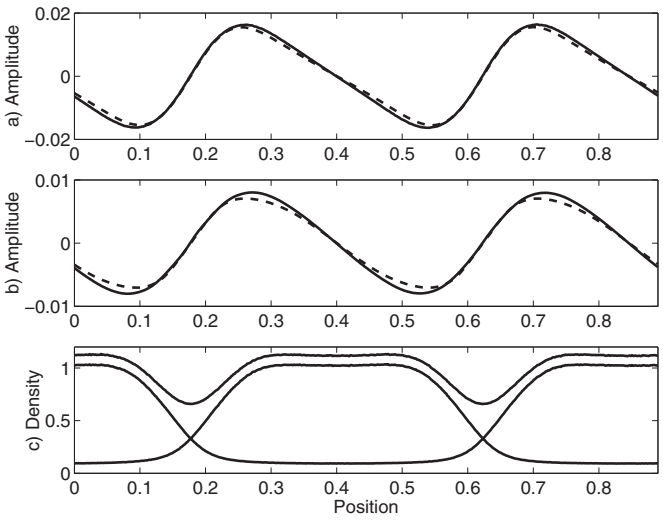

FIG. 2. (a) The $E_x(x,t=56)$ (dashed curve) and $2E_B(x,t=56)$ (solid curve). (b) The time-averaged $\tilde{E}_x$ (dashed curve) and $\tilde{E}_B$ (solid curve). (c) The number densities for $t=56$ normalized to $2n_e$ of both beams separately (beam 1 is almost confined to $0.2<x<0.6$) and both densities added together.

by the FI along x. The charge-neutral and current-neutral plasmas are transformed into one with $J_z(x)\neq 0$. The z-component of Ampere's law is in the 1D geometry $\partial_x B_y = J_z + \partial_t E_z$. A $J_z \propto \sin(kx)$ gives a $E_z \propto \sin(kx)$ and $B_y \propto -\cos(kx)$ so that E_z and B_y will have a phase shift of 90°. Figure 1 reveals this phase shift between B_y and the evanescent E_z. It also shows that an electrostatic E_x-field grows. The $B_y(x,t)$ and the $E_x(x,t)$ oscillate in space with the wave numbers k_1 and k_2, respectively, where $k_j = 2\pi j/L$. Both fields are spatially correlated. The comparison of E_x and B_y at $t=56$ demonstrates that $E_x=0$ if $B_y=0$ or if $d_x B_y=0$.

We determine now the relation between E_x and B_y. Let $E_B(x,t)$ be an electric field along x, which exerts the same force on an electron as the magnetic pressure gradient force does. This electric field is given in our normalization (charge $q=-1$) as $E_B(x,t)=-B_y(x,t)d_x B_y(x,t)$. We note that $B_y(x,t>56)$ is quasistationary while $E_x(x,t>56)$ oscillates in time. The oscillation amplitude of $E_x(x,t>56)$ is approximately constant and it apparently oscillates around a stationary background field. It is helpful to average the $E_x(x,t)$ and the $E_B(x,t)$ over the time interval $t_1=56$ to $t_2=125$ to give $\tilde{E}_x(x)=(t_2-t_1)^{-1}\int_{t_1}^{t_2} E_x(x,t)dt$ and $\tilde{E}_B(x)=(t_2-t_1)^{-1}\times\int_{t_1}^{t_2} E_B(x,t)dt$.

Figure 2(a) displays the $E_x(x,t=56)$ when the FI has just saturated and reached its peak amplitude and it compares it with $E_B(x,t=56)$. It turns out that $E_x(x,t=56)\approx 2E_B(x,t=56)$. The time-averaged fields fulfill $\tilde{E}_x(x)\approx\tilde{E}_B(x)$ in Fig. 2(b). The $E_x(x,t>56)$ oscillates in time with an amplitude $\approx\tilde{E}_B(x)$ around a stationary background field with the amplitude $\approx\tilde{E}_B(x)$. Both amplitudes add up to $2\tilde{E}_B(x)$ at $t=56$. When the oscillatory and the background electric field have a phase shift of 180° in time, they result in a $E_x(x,t_c)\approx 0$, for example, when $t_c=75$ in Fig. 1(b).

The $E_B(x,t=56)$ and $\tilde{E}_B(x)$ correlate well in Fig. 2(c) with the normalized number density distributions $n_{1,2}(x) = (2n_e)^{-1}\int f_{1,2}(x,\boldsymbol{p})d\boldsymbol{p}$ of each beam and also with the summed distribution $n_1(x)+n_2(x)$ at $t=56$. The total density is modulated by about 30%, while that of n_1 and n_2 varies by an order of magnitude.

Figure 3 shows the electron phase space distributions $f(x,p_z)$ and $f_i(x,p_x)$ at $t=56$. The mean velocity along z of the electrons of the beams 1 ($i=1$) and 2 ($i=2$) is practically constant as a function of x. Any spatial modulation would be caused by the $\boldsymbol{E}\times\boldsymbol{B}$-force, which is given by the product of E_x and B_y in our geometry. The effects of this force are small. The supplementary movie animates in time the $f_1(x,p_x,t)$ and $f_1(x,p_z,t)$ of beam 1, where the color scale denotes the

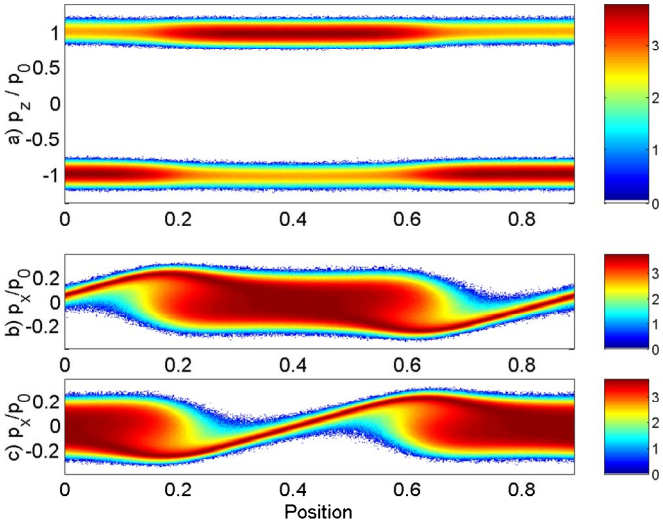

FIG. 3. (Color online) The ten-logarithmic phase space densities in units of CPs at $t=56$: Panel (a) shows the $f(x,p_z)$ with $p_0=m_e v_b \Gamma(v_b)$. The temperature and the mean velocity along z of the electrons are unchanged as a function of x. The density oscillates by the factor ≈ 10. The $f_1(x,p_x)$ is shown in (b) and the $f_2(x,p_x)$ in (c) (enhanced online).[URL: http://dx.doi.org/10.1063/1.3160629.1]

Downloaded 23 Aug 2011 to 143.117.13.152. Redistribution subject to AIP license or copyright; see http://pop.aip.org/about/rights_and_permissions

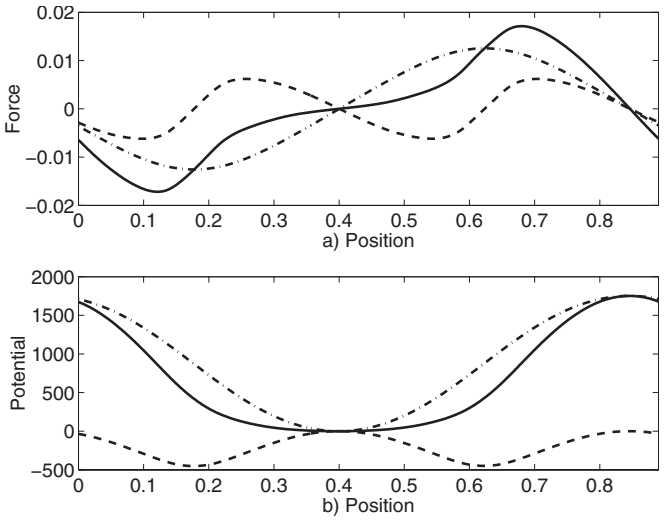

FIG. 4. The fields $\tilde{E}_j$ and the potentials $\tilde{U}_j$ averaged over $68<t<125$: (a) shows $\tilde{E}_x$ (dashed), $\tilde{E}_D=-v_b\tilde{B}_y$ (dashed dotted), and $\tilde{E}_T=\tilde{E}_x+\tilde{E}_D$ (solid line). Positive $\tilde{E}_j$ accelerate electrons into the negative x-direction. (b) shows the potential $\tilde{U}_x$ (dashed), $\tilde{U}_D$ (dashed dotted), and the $\tilde{U}_T$ (solid). The potential at $x_e=0.4$ is the reference potential.

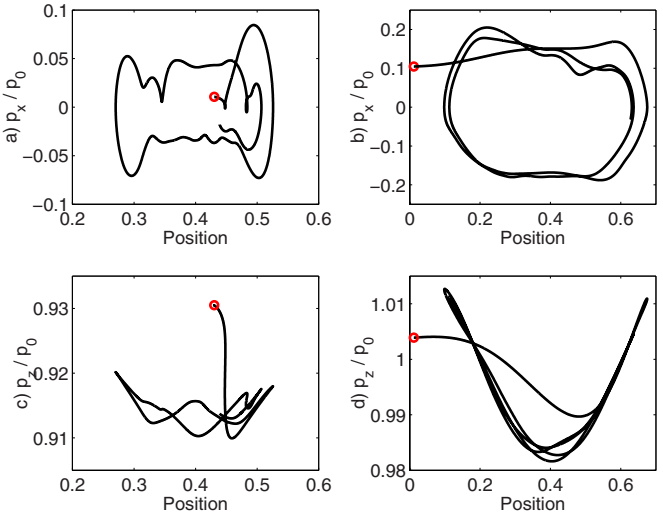

FIG. 5. (Color online) The trajectories of two selected CPs: (a) and (c) show the x,p_x and x,p_z diagrams of the CP 1. (b) and (d) show the corresponding diagrams for the CP 2. The circle denotes the starting point of the trajectory. Both CPs follow straight paths in the x,p_x plane for $0.33<x<0.47$ and they are rapidly reflected outside this interval.

ten-logarithmic number of CPs. The electrons are redistributed along x but they keep their p_z almost unchanged. Their flow along x oscillates, giving a $J_x(x,t)\neq 0$. The $f_1(x,p_x,t)$ reveals a dense electron core and two phase space vortices, which rotate around the equilibrium point $x_e=0.4$ with $E_x(x_e)=B_y(x_e)=0$ (see Fig. 1). These electrons are trapped by a potential.

We can estimate the contributions of E_x and B_y to this potential after the saturation of the FI. We average the fields $\tilde{E}_x(x)=(t_2-t_1)^{-1}\int_{t_1}^{t_2}E_x(x,t)dt$ and $\tilde{B}_y(x)=(t_2-t_1)^{-1}\int_{t_1}^{t_2}B_y(x,t)dt$ in time from $t_1=68$ to $t_2=125$. In what follows we consider beam 1 with $v_b>0$. According to the supplementary movie, most of the electrons have the velocity components $v_z\approx v_b$ and $v_x\ll v_b$. The electrons retain their initial $v_y\ll v_b$, since no force component along y develops. The dominant component of the time-averaged magnetic force is thus $\tilde{F}_x=v_b\tilde{B}_y$ for $q=-1$. The time-averaged force along x is then $\tilde{F}_x=-(\tilde{E}_x+\tilde{E}_D)$ with $\tilde{E}_D=-v_b\tilde{B}_y$ and we define $\tilde{E}_T=\tilde{E}_x+\tilde{E}_D$. The time-averaged potentials $\tilde{U}_j(x)=U_{0,j}+\int_0^x\tilde{E}_j(\tilde{x})d\tilde{x}$ with the indices $j=x,D,T$ are calculated from these fields and $U_{0,j}$ is set such that $\tilde{U}_j(x_e)=0$. The potentials are given in volts.

Figure 4 displays the time-averaged fields and potentials. The $\tilde{E}_x$ destabilizes the equilibrium position x_e because the negative $\tilde{E}_x(x>x_e)$ close to x_e accelerates the electron in the positive direction and the positive $\tilde{E}_x(x<x_e)$ close to x_e in the negative direction. The $\tilde{E}_D(x\approx x_e)$ is confining the electrons around $x\approx x_e$. The $|\tilde{E}_D|>|\tilde{E}_x|$ for $x\approx x_e$ and E_T is thus a confining force. However, the electron acceleration at $x\approx x_e$ is decreased by $\tilde{E}_x$ and increased at larger $|x-x_e|$.

The CPs of the beam 1 should follow almost straight paths close to x_e and they should be rapidly reflected for $|x-x_e|>0.2$. The potential difference $\Delta_U=\max(\tilde{U}_T)-\min(\tilde{U}_T)\approx 1700$ V should trap electrons with speeds up to $\Delta_v=(2e\Delta_U/m_e)^{1/2}/v_b\approx 0.27$. This matches the momentum spread of the cool core population in Fig. 3. The oscillations of E_x in Fig. 1 and, thus, of the strength of the confining potential explain the periodic release of electrons from this cool core seen in the movie. The oscillatory force imposed on the electrons by $E_x(x,t)$ contributes to their heating.

Figure 5 follows the trajectories of two CPs of beam 1. The circles denote the times when the CPs start interacting with the fields and the trajectories are followed until $t=125$. The CP 1 has a low initial modulus of p_x and CP 2 a high one. Both CPs follow straight paths in the interval $0.33<x<0.47$, in which $\tilde{E}_T$ in Fig. 4 is small. The phase space path of the faster CP 2 is smoother than that of CP 1. The low speed of CP 1 implies a long crossing time of the interval with a low modulus of $\tilde{E}_T$ and the CP 1 experiences several oscillation cycles of E_x. Both CPs are reflected outside the interval $0.33<x<0.47$ and they remain trapped because they cannot overcome the potential difference Δ_U. Both electrons change their v_z only by a few percent and $|v_x|<v_b/5$, which is supporting our previous assumption of a dominant and constant force $v_b\tilde{B}_y$ along x.

In summary, we have examined the saturation of the FI driven by two counterpropagating, weakly relativistic, and symmetric beams of electrons. The 1D simulation box has been oriented orthogonally to $\boldsymbol{v}_b$. It can approximate the quasiplanar boundary between two filaments with oppositely directed flow, which shows up if the magnetic confinement cannot overcome the thermal pressure. This geometry is beneficial because two of the three spatial derivatives in the Maxwell equations vanish, which separates the electrostatic and the electromagnetic fields.

We have confirmed that the electrostatic field, which grows during the nonlinear phase of the FI and for the initial conditions we consider, is driven by the magnetic pressure gradient. This has been proposed elsewhere[15,18] but a quantitative comparison has so far been lacking. We have shown

Downloaded 23 Aug 2011 to 143.117.13.152. Redistribution subject to AIP license or copyright; see http://pop.aip.org/about/rights_and_permissions

with a PIC simulation that the force imposed on an electron by the time-averaged electrostatic field $\tilde{E}_x(x)$ matches the $\tilde{E}_B(x)$, which results from the time-averaged magnetic pressure gradient force. The $E_x(x,t)$ is, however, not time stationary, which can be explained as follows.

The FI accelerates through the magnetic pressure gradient force the electrons and a current $J_x(x,t)$ builds up. The J_x can be cancelled by positrons[22] because the magnetic pressure gradient force does not depend on the sign of the charge. A $J_x \neq 0$ results with $\nabla \times \boldsymbol{B}=0$ (1D) through $J_x(x,t) = -\partial_t E_x(x,t)$ in a growing $E_x(x,t)$. Initially, $E_x(x,t=0)=0$ and $J_x(x,t=0)=0$. Any oscillatory solution for $J_x(x,t)$ and $E_x(x,t)$ implies through $J_x(x,t)=-\partial_t E_x(x,t)$ that J_x and E_x cannot simultaneously oscillate in time around their initial values. The $E_x(x,t)$ oscillates instead around its time average, which is the background field $\tilde{E}_B(x)$. The oscillation amplitude of E_x is approximately $\tilde{E}_B(x)$. The superposed oscillatory and background field thus oscillate between $E_x(x)=0$ at certain times t, fulfilling also the initial condition at $t=0$, and a maximum $E_x(x)=2\tilde{E}_B(x)$. The $\tilde{E}_B$ will eventually accelerate the ions.[10] However, the dynamical interplay of the filaments in 2D will also become important[16,17] on such time scales.

We have confirmed previous suggestions that the electric force is comparable to the magnetic field force.[10,13] We have used the time-averaged electric and magnetic forces to estimate their effects quantitatively. The electric field repels electrons at the filament centers and attracts them if they are farther away, which permits filaments to overlap. The repulsive electric field limits the peak (current) density of the filaments compared to those composed of electrons and positrons. The latter can thus sustain larger magnetic field gradients.[22]

The authors acknowledge the financial support by an EPSRC Science and Innovation award, by the visiting scientist program of the Queen's University Belfast, by Vetenskapsrådet, and by the DFG (Grant No. Forschergruppe FOR1048).

[1] T. Y. B. Yang, Y. Gallant, J. Arons, and A. B. Langdon, Phys. Fluids B **5**, 3369 (1993).
[2] Y. Kazimura, J. I. Sakai, T. Neubert, and S. V. Bulanov, Astrophys. J. **498**, L183 (1998).
[3] M. V. Medvedev and A. Loeb, Astrophys. J. **526**, 697 (1999).
[4] S. Zenitani and M. Hesse, Phys. Plasmas **15**, 022101 (2008).
[5] M. Swisdak, Y. H. Liu, and J. F. Drake, Astrophys. J. **680**, 999 (2008).
[6] M. Karlicky, D. H. Nickeler, and M. Barta, Astron. Astrophys. **486**, 325 (2008).
[7] M. Tabak, J. Hammer, M. E. Glinsky, W. L. Kruer, S. C. Wilks, J. Woodworth, E. M. Campbell, M. D. Perry, and R. J. Mason, Phys. Plasmas **1**, 1626 (1994).
[8] R. B. Campbell, R. Kodama, T. A. Mehlhorn, K. A. Tanaka, and D. R. Welch, Phys. Rev. Lett. **94**, 055001 (2005).
[9] A. Bret, L. Gremillet, and J. C. Bellido, Phys. Plasmas **14**, 032103 (2007).
[10] F. Califano, T. Cecchi, and C. Chiuderi, Phys. Plasmas **9**, 451 (2002).
[11] R. C. Davidson, D. A. Hammer, I. Haber, and C. E. Wagner, Phys. Fluids **15**, 317 (1972).
[12] R. Lee and M. Lampe, Phys. Rev. Lett. **31**, 1390 (1973).
[13] M. Honda, J. M. ter Vehn, and A. Pukhov, Phys. Rev. Lett. **85**, 2128 (2000).
[14] J. I. Sakai, R. Schlickeiser, and P. K. Shukla, Phys. Lett. A **330**, 384 (2004).
[15] A. Stockem, M. E. Dieckmann, and R. Schlickeiser, Plasma Phys. Controlled Fusion **50**, 025002 (2008).
[16] M. V. Medvedev, M. Fiore, R. A. Fonseca, L. O. Silva, and W. B. Mori, Astrophys. J. Lett. **618**, L75 (2005).
[17] M. E. Dieckmann, I. Lerche, P. K. Shukla, and L. O. C. Drury, New J. Phys. **9**, 10 (2007).
[18] G. Rowlands, M. E. Dieckmann, and P. K. Shukla, New J. Phys. **9**, 247 (2007).
[19] J. M. Dawson, Rev. Mod. Phys. **55**, 403 (1983).
[20] J. W. Eastwood, Comput. Phys. Commun. **64**, 252 (1991).
[21] L. O. Silva, AIP Conf. Proc. **856**, 109 (2006).
[22] M. E. Dieckmann, P. K. Shukla, and L. Stenflo, Plasma Phys. Controlled Fusion **51**, 065015 (2009).

Downloaded 23 Aug 2011 to 143.117.13.152. Redistribution subject to AIP license or copyright; see http://pop.aip.org/about/rights_and_permissions